



Resolvent Analysis of Hypersonic Boundary Layer over Blunted Cones

Thomas Lescop ¹, Julien Lefieux ²
MBDA France, 1 Av. Réaumur, 92350 Le Plessis-Robinson, France

Guillaume Bégou ³ Cédric Content ⁴ Nicolo Fabbiane ⁵ Pierre Nibourel ⁶ Reynald Bur ⁷ DAAA, ONERA, Institut Polytechnique de Paris, F-92190 Meudon - France

Abstract

The stability of hypersonic boundary layers, though well documented by both experimental and numerical studies on flat-plates and sharp geometries, is still not fully understood on blunted geometries. But robust previsions of the transition onset are however crucial to the design of hypersonic vehicles, which are often blunted. This geometry change is known to modify the physical mechanisms behind transition, favouring non-modal amplification of convective instabilities over boundary-layer modes like the 1^{st} and 2^{nd} Mack modes which dominate in hypersonic flows over sharp geometries.

In this work, the boundary-layer stability over 5° blunted cones with no Angle of Attack (AoA) is investigated numerically in a linear framework, by means of Resolvent (Input/Output) Analysis. The goal of this study is to assess how moderate nose bluntness can delay transition and set up a robust methodology based on the semi-empirical N factor metric to locate the transition onset to turbulence.

To validate the methodology, a 2^{nd} mode dominated sharp test case at Mach 6 and unit Reynolds number of 11.15 millions is used to compare Resolvent to Parabolised Stability Equations (PSE) results from the literature. Then the parametric study on bluntness effects is carried out with Mach and unit Reynolds numbers of 6 and 4.279 millions respectively, on 0.1, 1, 2.5 and 5mm nose radii. All cases fall below the Transition Reversal regime at their respective unit Reynolds numbers. With a total temperature of 430K for the freestream flowfield, the high enthalpy and real gas effects are not considered in this work. Considering their respective hypothesis, the Resolvent results compare well with the PSE predictions. Increasing bluntness has been found to suppress the 2^{nd} mode very heavily in comparison to the 1^{st} mode, while the streaks are not damped and become the dominant instability.

Keywords: Hypersonic, Boundary Layer, Stability

1. Introduction

In hypersonic flight, aircrafts experience severe thermal loads which can lead to the ruin of the structure if not properly dealt with. Consequently, the accurate estimation of wall heat fluxes is crucial for the design of the vehicles' thermal protection systems. Among other phenomena, transition to turbulence has a significant impact on aerothermal heating, as turbulent boundary layers generate significantly larger heat transfer rates than the ones generated by laminar boundary layers [1]. Additionally, an incorrect appreciation of the boundary-layer's state impacts the skin friction prediction and eventually the efficiency of downstream control surfaces.

Transition to turbulence originates from small amplitude perturbations in the ambient air flow which are

¹PhD Candidate, thomas.lescop@mbda-systems.com

²Research Engineer, julien.lefieux@mbda-systems.com

³Research Engineer, guillaume.begou@onera.fr

⁴Research Engineer, cedric.content@onera.fr

⁵Research Engineer, nicolo.fabbiane@onera.fr

⁶Research Engineer, pierre.nibourel@onera.fr

⁷Research Director, reynald.bur@onera.fr

filtered across the boundary layer through mechanisms of receptivity. From a dynamical system point of view, the boundary layer behaves like a selective noise amplifier, therefore these filtered perturbations trigger convective instabilities that can experience modal and/or non-modal growth, up until non-linear effects emerge and lead to the turbulent breakdown. Considering not only free-stream turbulence but also potential acoustic or entropic perturbations, the non-linear effects will take the lead on linear ones with increasing disturbance levels in the incoming flow [2]. In flight conditions, these levels remain relatively low and most of the transition process (before breakdown) can thus be described in a linear framework. In hypersonic flows, this linear path to turbulence has been extensively described and explained both experimentally and numerically, on geometries such as flat plates and sharp cones. An exhaustive literature review can be found in [3]. Transition is there dominated by modal instabilities such as the 1^{st} and 2^{nd} Mack modes, respectively above and below Mach 4 [4]. However these flows differ from the ones relevant for industrial applications in several key aspects such as surface roughness, high enthalpy effects, or bluntness effects.

This work focuses on the impact of the latter, without taking into account the two former. In the case of a blunt cone, the flow topology changes drastically in comparison to a sharp one as a detached bow shock forms around the nose, creating a zone of high entropy gradient. These gradients generate a rotational flow, which can enter the boundary layer and affect its development [5]. From a stability point of view, the bluntness effects heavily damp the 2^{nd} Mack mode because of the favourable pressure gradient. Transition is therefore repelled downstream. But experimental work [6, 7] has shown that this trend slows down as the nose radius increases and eventually reverses, leading to the so-called "Transition Reversal" phenomenon. This change in behaviour cannot be predicted by modal analysis [8] and could be linked to the transient growth of instabilities evolving in the entropy layer [9]. This research also reveals a range of moderate nose bluntness where the modal growth is overtaken by transient growth even before the actual "Transition Reversal". By means of Non-linear Parabolised Stability Equations (NPSE) and Direct Numerical Simulations (DNS) it has now been shown that these non-modal instabilities in the entropy layer can trigger transition through secondary non-linear interactions [10].

Consequently the stability results presented in this work have been obtained by means of Resolvent (Input/Output) Analysis, which is suitable to detect modal and non-modal convective instabilities in a global linear framework. The studied geometry is the cone of the Cone-Cylinder-Flare at 12° model [11], latter referred to as CCF 12, which is a geometry specifically designed to study convective and global instabilities. Our goal is to explore the aforementioned moderate nose bluntness range by highlighting the mechanisms leading to the offset of the transition, and set up robust method to predict transition in this range. A significant part of this work is devoted to the adaptation of the semi-empirical e^N method [12, 13], initially developed for Linear Stability Theory (LST), in the context of Resolvent Analysis.

The layout of the paper is as follows. First the governing equations relevant to the Resolvent Analysis are introduced in Section 2. Then the method developed to predict transition to turbulence is explained from the computation of the baseflow in Section 3 to the stability and N factor calculations in Section 4. Section 5 presents a validation of the methodology on a sharp case at Mach 6 and unit Reynolds number of 11.15 millions, where N factors computed via Resolvent Analysis are compared to the ones computed via PSE from [11]. Finally Section 6 sheds light on the competition between modal and non-modal growth in the moderate bluntness range.

2. Governing Equations

In this section the theoretical developments used to compute a baseflow and obtain stability results by means of Resolvent Analysis are described. Consider $q = [\rho, \rho u, \rho v, \rho w, \rho E]^T$ the vector of conservative variables where ρ is the density, $\rho u, \rho v, \rho w$ the momentums in the axial, radial and azimuthal directions respectively, and ρE the energy stagnation density. Since this work only involves flows over a cone with no AoA we consider the 2D-axisymetric form of the Navier-Stokes equations, with a small amplitude forcing term f':

$$\frac{\partial q}{\partial t} = \mathcal{N}(q) + f' \tag{1}$$

The forcing term is added because the undisturbed system is stable. This kind of flow has been shown to be globally stable so we call fixed-point \overline{q} the laminar solution of the undisturbed Navier-Stokes system,

thus verifying $\mathcal{N}(\overline{q})=0$. Adding a 3D perturbation to the 2D fixed point, the conservatives vector now reads:

$$q(x, y, z, t) = \overline{q}(x, y) + q'(x, y, z, t)$$
(2)

As this perturbation is of small amplitude $\|q'\|/\|\overline{q}\| << 1$, one can linearise the Navier-Stokes systems around the fixed-point after combining Eq.1 and Eq.2. Keeping only the first order terms, the linearised system can now be written as:

$$\frac{\partial q'}{\partial t} = \mathcal{J}q' + f' \tag{3}$$

With $\mathcal{J}=\frac{\partial \mathcal{N}(q)}{\partial q}|_{\overline{q}}$ the Jacobian operator resulting from the linearisation around the fixed-point. One can then apply a Fourier transform to the perturbation and the forcing, which then reads:

$$q' = \hat{q}(x,y)e^{i(m\theta+\omega t)} + c.c.$$

$$f' = \hat{f}(x,y)e^{i(m\theta+\omega t)} + c.c.$$
(4)

Eq.4 can then be injected into Eq.3 to obtain the so called Input/Output relation:

$$\hat{q} = \mathcal{R}\hat{f} \tag{5}$$

Where $\mathcal{R}=(i\omega\mathbf{Id}-\mathcal{J})^{-1}$ is the Resolvent operator, which acts like a transfer function between the forcing and the perturbation response. We then set up an optimisation problem to compute the optimal gain for each couple (ω,m) of interest:

$$\mu^{2}(\omega, m) = \max_{f'} \frac{\|\hat{q}\|^{2}}{\|\hat{f}\|^{2}} \tag{6}$$

Because the optimal perturbation can be supported by several components of the conservatives vector, one needs to choose the appropriate norm to perform the optimisation. For compressible flows such as here, Chu's [14] norm seems to be the most appropriate, as it takes into account both the kinetic and thermodynamic components of the perturbation. In its dimensional form, the volumic Chu energy reads:

$$dE_{Chu}(\omega, m) = \frac{1}{2}\overline{\rho} \|V'\|^2 + r \frac{\overline{T}}{\overline{\rho}} (\rho')^2 + \frac{r}{\gamma - 1} \frac{\overline{\rho}}{\overline{T}} (T')^2$$
(7)

And the response's norm corresponds to its value integrated in the whole domain:

$$E_{Chu}(\omega, m) = \int_{\nu} dE_{Chu} d\Omega \tag{8}$$

To solve Eq.6, the gain is computed with the norm matrix Q_E and Q_F for the response and forcing respectively. Their expressions can be found in [15] and allow to turn the optimisation problem into a Global Hermitian Eigenvalue Problem (GHEP) by injecting Eq.5 into Eq.6:

$$\mathcal{R}^* \mathcal{Q}_E \mathcal{R} \hat{f} = \mu^2 \mathcal{Q}_F \hat{f} \tag{9}$$

The superscript * denotes the conjugate transpose.

3. Baseflow Computation

This section describes the methodology and codes used to compute the baseflow and perform the aforementioned stability calculations for all the presented results. Since hypersonic flows around sharp and blunted cones are globally stable, one can compute a stationary fixed point which verifies $R(\hat{q})=0$. R being the residual of the undisturbed Navier-Stokes system (same as in Eq.1 but without the forcing term f'). This baseflow is computed using a Relaxed Newton method initialised with a solution obtained by a Time-Stepping solver. Once obtained, Resolvent Analysis can be performed to identify the linear instabilities potentially involved in the transition to turbulence.

3.1. Meshes and boundary-conditions

The mesh used for all the presented results have the same characteristic as the one described in this section. We use a 2D body-fitted structured mesh, which is also shock-fitted. The original CCF 12 model is 15.72in (399mm) long cone, with a 5° half-angle and a 0.1mm nose radius. It will be referred to as the "sharp" model, in opposition to the blunted ones with 1mm, 2.5mm and 5mm nose radii. Because of the axisymetry of the geometry and the zero AoA, only half a slice of the cone is actually computed as shown in Fig.1.

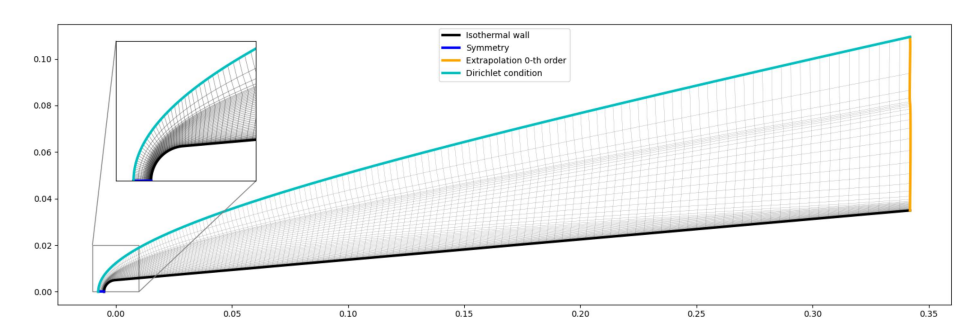


Fig 1. Mesh and boundary-conditions of the 5 mm blunt cone. Only one cell out of ten is shown.

From the wall to the shock, the normalwise distribution is linear then bi-geometric to ensure a satisfactory refinement in the boundary layer and near the shock. From the shock to the farfield boundary-condition, the distribution is geometric. For all meshes used in this work, the normalwise discretisation is composed of 50 points above the shock and 400 below it. These meshing guidelines have been shown to allow for the convergence of optimal responses on similar baseflows [16, 17]. For the streamwise direction, the spherical part of the cone is composed of $N_n=100\times\sqrt{R_n/10^{-4}}$ uniformly distributed points and a linear distribution is applied on the frustum to ensure the continuity of the streamwise mesh size at the nose-frustum interface as well as a prescribed cell length at the end of the cone. This length is calculated so that the spatial wavelength of the highest frequency instability which we aim to study, i.e the 2^{nd} Mack mode, is discretized by 12 cells to fit the mesh convergence criterion proposed by [18]. Because the 2^{nd} Mack mode frequency can be approximated as $f_{2nd} \approx u_e/2\delta$ [19] and the laminar boundary-layer height scales as $\delta(x) \propto x/\sqrt{Re_x}$ [20], one can write:

$$f_{2nd} \propto rac{u_e\sqrt{Re}}{2\sqrt{x}}$$
 (10)

And as u_e depends on the free-stream velocity where viscous effects are negligible, it can be assumed constant at the end of the cone. Consequently, maintaining a constant number of cells per spatial wavelength of the 2^{nd} Mack mode at the end of the cone while increasing Re unit leads to an increase in cell number proportional to the square root of the new Re over the initial one. The respective mesh sizes of the discussed cases are listed in Table 1.

Case name	Nose radius [mm]	R _e unit	N _{sphere}	N _{cone}
Valid0.1	0.1	11.15×10^6	100	2630
Sharp0.1	0.1	4.279×10^{6}	100	1625
Blunt1	1	4.279×10^{6}	315	1585
Blunt2.5	2.5	4.279×10^{6}	500	1515
Blunt5	5	4.279×10^{6}	705	1395

Table 1. Streamwise mesh discretisation.

At the wall, a no-slip isothermal boundary condition is enforced at 300K, the other ones are also displayed in Fig.1.

3.2. Relaxed Newton

A detailed description of the Relaxed Newton method and associated solver can be found in [18], we only give an overview here. To initialize it a time marching solver included in BROADCAST is used. Several successive computations are required to iteratively localize and refine the shock area. The convective fluxes are reconstructed using a 7th order accurate directional FE-MUSCL scheme and the viscous fluxes with a 4th order compact scheme. Finally the solution is converged down to machine precision with BROADCAST's Relaxed Newton mode. As suggested by its name, the method consists in the local linearisation of the problem to calculate the state vector increment δq^n supposing that $\mathrm{R}(q^{n+1})=0$. The recurrence relation reads:

$$\begin{cases} (\frac{1}{\Delta t^n} + \mathcal{J}(q^n))\delta q^n = -\mathbf{R}(q^n) \\ q^{n+1} = q^n + \delta q^n \end{cases} \tag{11}$$

Where Δt^n is the relaxation term, linearly depending on the CFL. Note that $\mathcal{J}(q^n)$ is the full Jacobian operator evaluated at q^n and is extracted through Algorithmic Differentiation. The fixed point is considered converged when a plateau is reached, where the residuals are not concentrated in high gradients area such as in the shock, but only correlated with the size of the considered cells.

4. Stability Analysis

Once the baseflow is computed, the stability calculations mentioned in Section 2 are conveyed following the procedure described in this section.

4.1. Resolvent Analysis

As mentioned before the GHEP Eq.9 allows the calculation of the most energetic responses for a forcing of given temporal and azimuthal (spatial) frequency. Several algorithms can be employed to solve such large GHEP, here the Krylov algorithm described in [21] is used. One can therefore map the instabilities that could be sustained in the considered flow, and most importantly those which could experience significant growth if introduced in the boundary layer. An example of such optimal gain map is depicted in Fig.6, where 1^{st} and 2^{nd} Mack modes clearly appear as well as streaks.

In this work, no assumptions are made about the receptivity of the studied boundary layers. Therefore the optimisation problem Eq.6 is solved with a 5 degrees of freedom forcing (on each of q' components) and without restricting it to a particular zone of the computational domain. Also if the whole range of studied (f,m) couple are considered as likely to occur in the flow, the comparison of optimal gains can then inform on the probability that one instability develops instead of another. But the same cannot be said about the probability that one instability actually leads to transition, as discussed in Section 4.3. In the following sections, we will mostly consider the largest eigenvalue μ_0 .

4.2. Kriging

As the Jacobian scales in $N\times N\times 5$ for a number of cells N, the resolution of the GHEP quickly becomes computationally intensive although $\mathcal J$ is extremely sparse. Therefore a compromise must be chosen between the map precision and its computational cost. Instead of a classic interpolation on a predefined grid in the (f,m) space the strategy described here uses Kriging, a stochastic interpretation of interpolation. The main point of this approach being that it allows one to quantify the uncertainties and infill new points where the metamodel is lacking.

First an initial dataset of (f,m) couples are computed to perform a preliminary screening of the optimal gains in the studied range of frequencies. This Design of Experiment (DOE) takes the form of a Latin Hypercube, as it shows great space-filling properties while avoiding the "curse of dimensionality". This Latin Hypercube Sampling (LHS) procedure is optimised to maximise the distance between each couple (f,m). Then the DOE can be in-filled in specific zones of interest (i.e containing several optimal gain peaks) detected by the initial screening. In this exploratory phase, the candidates are still chosen to maximise the distance between each sample in the parameters space. Then comes the maxima research phase, aiming at localising precisely the instabilities of interest. The design of experiments (DOE) is enriched by sampling locations that maximize the Expected Improvement (EI) criterion. In short, it is a trade-off between exploration (adding points in sparsely sampled regions) and exploitation (refining the search in the vicinity of predicted optima of the kriging surrogate).

The theory behind Kriging, DOEs and infill methods are overlooked here for the sake of concision, but an exhaustive review of these tools can be found in [22].

4.3. N factor

Once the instabilities likely to develop in the studied flow are identified and localised, one can access the optimal (and eventually suboptimal) gain and corresponding eigenvector \hat{q}_0 of the most amplified instability. But the link between these instabilities and the transition to turbulence is yet to be established. This link is based on the semi-empirical N factor theory, which is presented in this section. To begin with, one can express the perturbation's amplification rate from its amplitude A:

$$\sigma = \frac{1}{A} \frac{\partial A}{\partial s} \tag{12}$$

The N factor is then defined as the cumulative integral of the amplification rate along the streamwise direction. Knowing Eq.12, one can express this quantity as the exponential factor by which the initial amplitude A_0 of a perturbation introduced at the abscissa x_0 will be multiplied, once convected to the x abscissa:

$$N(x) = \int_{x_0}^{x} \sigma(s)ds$$

$$= \ln\left(\frac{A(x)}{A(x_0)}\right)$$
(13)

Consistently with the choice of the norm made in Section 2 and previous studies such as [9], the amplitude used here is the square root of the Chu energy integrated in the wall normal direction, which yields:

$$A(x) = \sqrt{\int_0^{+\infty} dE_{Chu} d\eta}$$
 (14)

One can note that N depends on x_0 , the position where the integration begins. As shown by previous comparisons between LST and Resolvent Analysis [23] the 2nd Mack mode's neutral point, *i.e* where it first becomes unstable in the sense of the LST, is coincident to the location of maximum forcing amplitude. Thus this is where x_0 is fixed for this work.

Several N factor curves can be computed for a single perturbation spanning over a range of significantly amplified (f, m) couples, in that case an envelope can be extracted. It has been experimentally shown that transition occurs at the location where the N factor envelope exceeds a transitional N factor value N_{tr} , which only depends on the test condition and facility, for a particular perturbation.

5. Validation

In this section the case Valid0.1 from Table 1 is discussed to compare the N factor computed in the Resolvent framework described in Section 4 and in the PSE framework of the STABL suite. The principle is to parabolize the linearized stability equations thanks to an ansatz which does not require the parallel flow hypothesis. More details about the PSE method are available in [24]. The N factors calculated by this means read:

$$N(x) = \int_{x_0}^{x} \left(-\alpha_i + \frac{1}{2E_k} \frac{\partial E_k}{\partial s} \right) ds$$
 (15)

Where α_R is the local streamwise wavenumber and E_k the disturbance kinetic energy.

Fig.2 shows N factor curves computed for the three most amplified frequencies of the 2^{nd} Mack mode at the end of the cone with both methods. The most unstable frequencies predicted by Resolvent and PSE Analysis are the same, at the end of the cone as well as on the frustum in general. But the N factors from Resolvent Analysis are significantly higher than the PSE ones. This can be explained by the non-modal component of the transient regime which generates the initial bump up to 0.2m on the Resolvent N factor curves, essentially giving it a head-start compared to the PSE which does not take this component into account. Moreover STABL considers the real gas effect and thermal/chemical non-equilibrium whereas our Resolvent methodology does not. However due to the low enthalpy of the free-stream conditions, these effects are not expected to yield significant differences in the results. It is also worth mentioning that these curves must be linked with their relative transitional N factor N_{tr} which is specific to the free-stream environment (*i.e* free-stream conditions and perturbation levels) and N factor computation method. Consequently, qualitative comparisons are preferred to quantitative ones when comparing such methods.

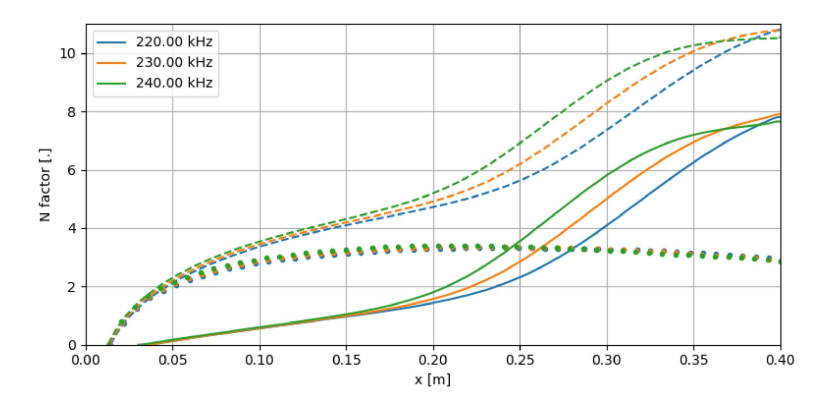


Fig 2. N factor curves computed by means of PSE (plain) and Resolvent (dashed) Analysis. The dotted curve is the difference between both curves.

6. Bluntness effects

The parametric study on the nose radius is now presented to assess bluntness effects on the flow stability. The maximum Re_{R_n} is 2.14×10^4 , which is far below the beginning of the Transition Reversal range [25]. The baseflows associated are displayed in Fig.3 for each nose radius. For the sharp case the entropy layer is overlapping the boundary layer on the whole frustum. For the blunt cases, it is eventually swallowed downstream, except for the 5 mm case where the end of the domain is reached before the entropy swallowing point.

The boundary layer, entropy layer and shock layer displayed are respectively defined as:

$$hi(\delta) = \frac{hi_{\infty} - hi_{w}}{0.995} + hi_{w}$$

$$\Delta s(\delta_{EL}) = 0.25 \Delta s_{w}$$

$$\frac{\partial \rho}{\partial \eta}(\delta_{SL}) = min(\frac{\partial \rho}{\partial \eta})$$
(16)

With the entropy increment defined as:

$$\Delta s = c_v \, \ln(\frac{\overline{T}}{\overline{T}_{\infty}}) - r \, \ln(\frac{\overline{\rho}}{\overline{\rho}_{\infty}}) \tag{17}$$

For all this section's results, the coordinates of the origin are shifted so that the end of each cone is displayed at the same coordinates as for the original CCF 12 geometry, *i.e* the sharpest case.

Fig.4 shows the evolution of the Mach number at the edge of the boundary layer. While it reaches a plateau almost immediately downstream of the sphere-frustum junction for the sharp case, two different zones can clearly be identified for the blunt cases. In the first one an intermediate plateau is reached around Mach 3, spreading further downstream of the junction with increasing nose radius. Then the edge Mach number increases to eventually reach the sharp case plateau. As long as the edge quantities, like the Mach, have not reached the sharp case plateau, one can argue that the boundary layer has not yet recovered from the influence of the entropy layer. It is also known that the non-uniformity of the

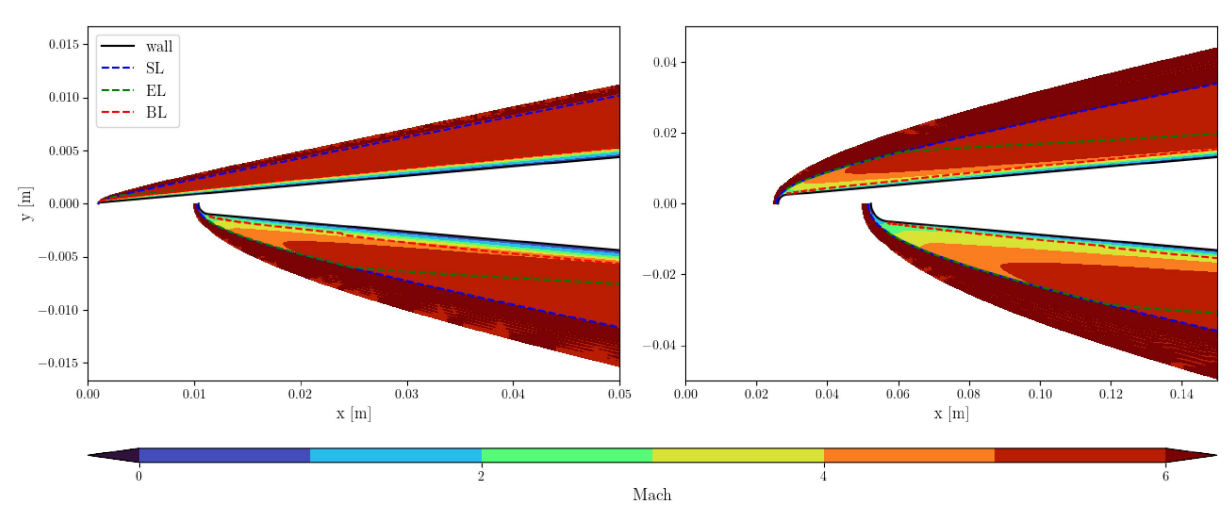


Fig 3. Mach number fields from the cases Sharp0.1 (top left), Blunt1 (bottom left), Blunt2.5 (top right) and **Blunt5** (bottom right) with the shock, entropy layer and boundary layer plotted (respectively abbreviated SL, EL and BL).

speed at the edge of the boundary layer on blunt cones is due to the speed gradient induced by the bow shock. Notably, Fig. 3 highlights that the junction between the two aforementioned zones is located where the entropy layer separates from the shock for all nose radii.

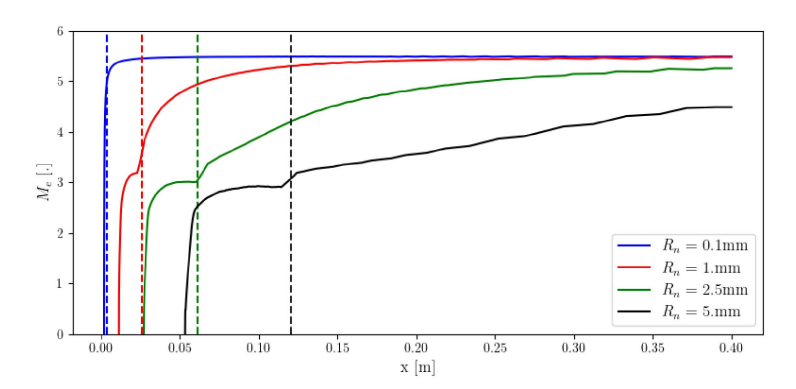


Fig 4. Mach number at the edge of the boundary layer on the whole domain length. The dashed lines correspond to the positions where the EL and SL separate for each case.

Fig.5 gives a 3D view of the response fields associated with the 2^{nd} and 1^{st} Mack modes as well as the streaks, on the sharp case. Note that the abscissa where the response appears is not where transition actually occurs as the scales were arbitrarily chosen for clarity, it is only displayed for illustrative purposes.

Fig.6 presents the optimal gain maps obtained for all 4 nose radii. The contour plots are the results of the Kriging prediction based on the depicted DOEs, as explained in Section 4.2.

As expected, the 1^{st} and 2^{nd} Mack modes fade away as the nose radius increases. For the latter, this can be explained by the decrease in edge Mach shown in Fig.4, as the 2^{nd} Mack mode dominates at higher Mach numbers. On the 5 mm case, only the streaks can clearly be distinguished. While the 2^{nd} Mack does not present a significant shift in its most amplified frequency, the 1^{st} does move to lower

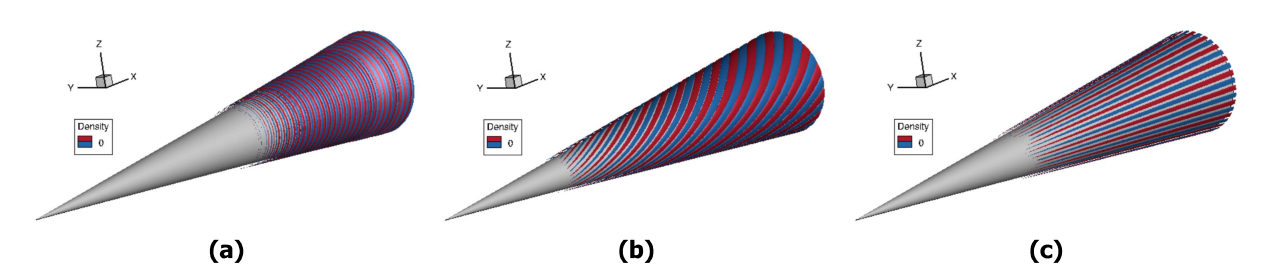


Fig 5. Response fields corresponding to the 2^{nd} (a) and 1^{st} (b) Mack modes as well as the streaks (c), on the case **Sharp0.1**.

frequencies and higher wavenumbers. Its increasing misalignment relatively to the mean flow seems to lead to a merging between the $\mathbf{1}^{st}$ Mack mode and the stationary streaks.

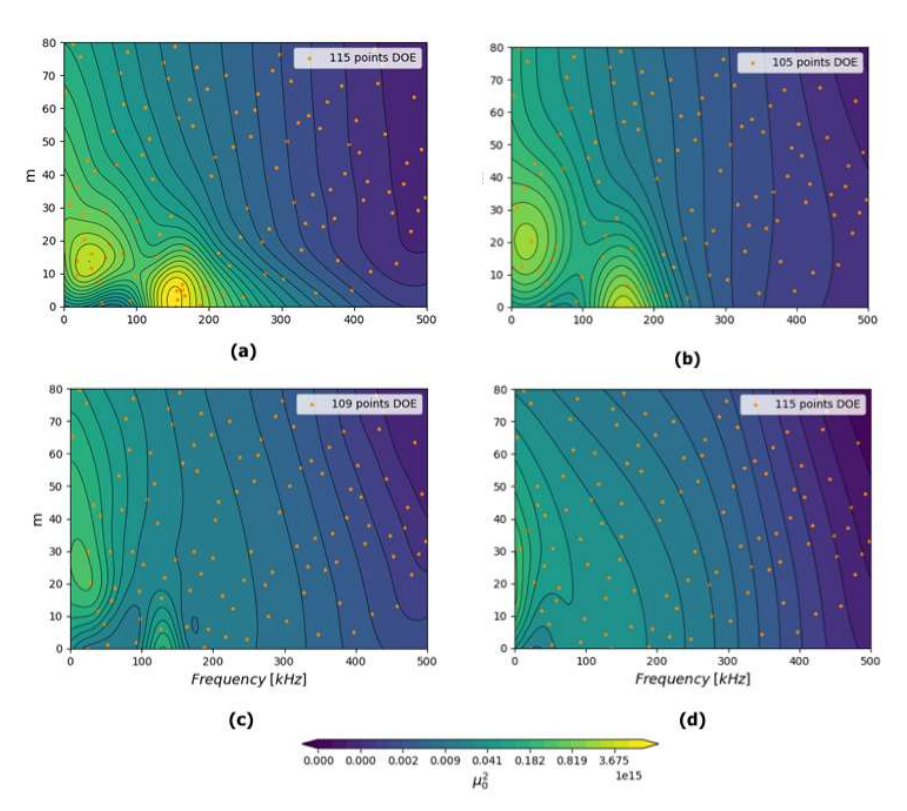


Fig 6. Gain maps corresponding to the 0.1mm (a), 1mm (b), 2.5mm (c) and 5mm (d). The light orange points correspond to the actually computed (f, m).

As the rest of this section focuses on the bluntness impact on the N factor curves, only the 0.1, 1 and 2.5mm cases will be treated as the 3 instabilities of interest cannot be clearly located on the 5mm case. As shown on Fig.7, the 2^{nd} Mack mode is the most impacted by the increasing nose radius. This heavy damping is due to a decreasing response amplitude but also to a downstream shift of the forcing, which is the most impactful as it delays the beginning of the N factor integration. This suggests that the increasingly large entropy layer dominated zone is not suited for the 2^{nd} Mack mode instability to develop. Consequently it is pushed downstream towards the swallowing point where the baseflow tends to its "sharp" profiles, more suited to its growth.

The 1^{st} Mack mode is also damped but this is mainly due to the decrease of the response amplitude, as the global maximum of the forcing amplitude remains close to the sphere-frustum junction. But it must

be noted that a local maximum further downstream is clearly visible and is affected by the increasing bluntness similarly to the 2^{nd} Mack mode's forcing amplitude. As explained in Section 4.3, the beginning of integration locus is defined as the maximum of forcing amplitude as it is coincident to the neutral point for the 2^{nd} Mack mode, but this assertion may not hold for the 1^{st} Mack mode. Therefore this analysis would benefit from further LST investigations to locate the 1^{st} mode's neutral point and correlate it with Resolvent associated variables.

For the streaks, the effects of bluntness is not clear but does not lead to a significant change in terms of N factors. Hence it can become the leading linear instability as the modes dominating sharp cases are suppressed by the increasing bluntness effects. Again the beginning of integration criteria may not be tailored for the streaks instability, but in this case LST investigations cannot be beneficial as it can only observe modal behaviours. Thus the neutral point would have to be located by means of non-modal analysis.

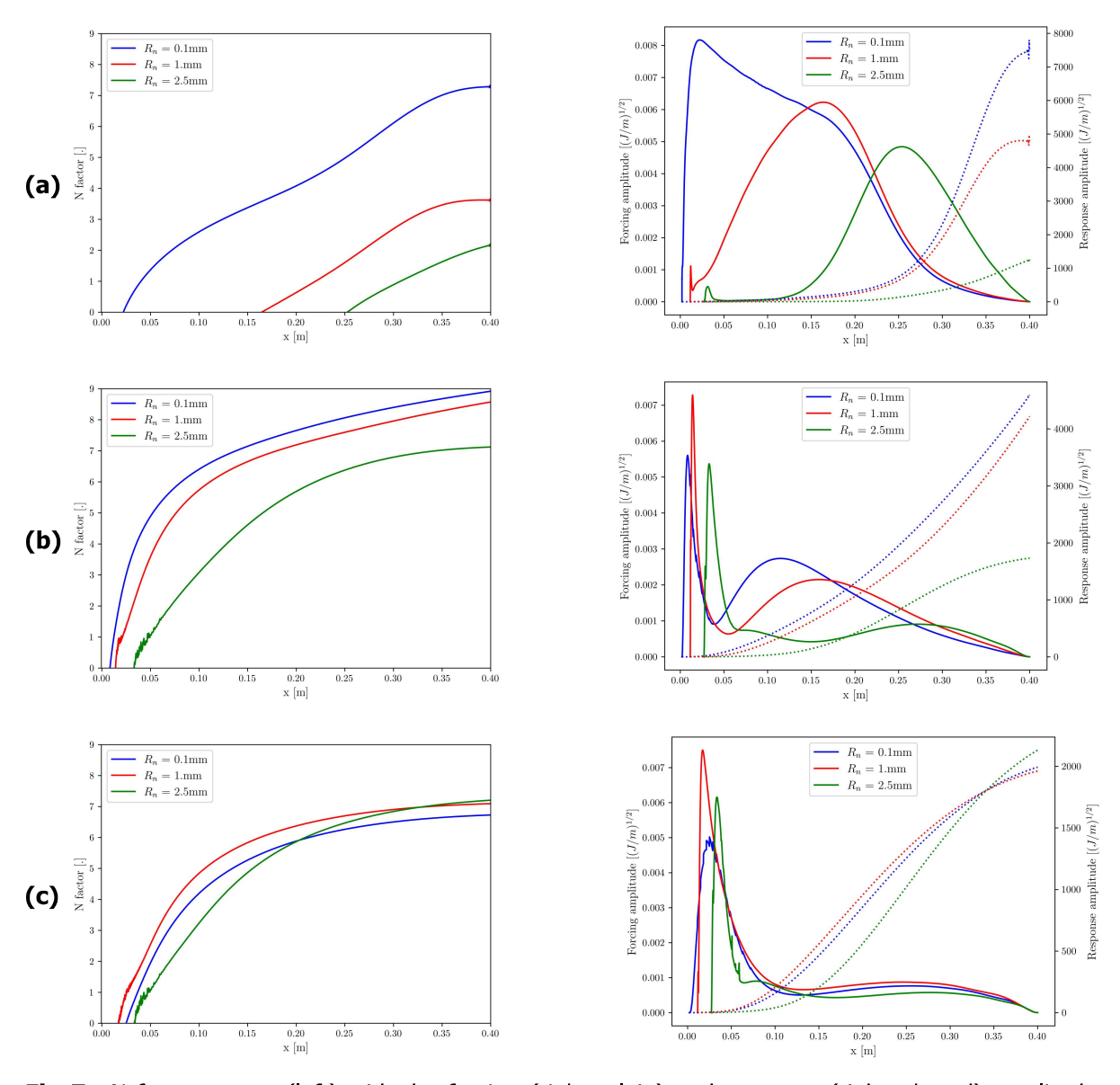


Fig 7. N factor curves (left) with the forcing (right, plain) and response (right, dotted) amplitudes corresponding to the most amplified (f,m) couples of the 2^{nd} Mack mode (**a**), the 1^{st} Mack mode (**b**), and the streaks (**c**).

7. Conclusion

The effects of bluntness on the stability of a hypersonic boundary layer over a blunt cone were assessed by means of Resolvent Analysis for several nose radii of moderate bluntness, with a nose radius based Reynolds number not exceeding $Re_{R_n}=2.14\times10^4$.

A robust methodology was also developed to predict transition onset in a linear framework, based on Resolvent Analysis and the N factors semi-empirical method. With the use of a Kriging metamodel, the associated workflow has proven its reliability to handle a wide range of flows over moderately blunt cones at Mach 6 for a relatively low computational effort. A validation case was run on a sharp cone to compare the N factor computed from Resolvent and PSE Analysis. The results showed a satisfactory agreement qualitatively, and also quantitatively in regards to the limitation of each tools.

It emerges that the Mack modes, usually dominant in boundary layers over sharp cones, are heavily damped with increasing nose bluntness. In particular, the impossibility for 2^{nd} Mack mode instabilities to develop in the boundary layer upstream of the entropy-layer swallowing point was highlighted. As a result the only significant linear instability remaining in the moderate bluntness regime are the streaks, which confirms previous assumptions citing it as a potential candidate to drive transition to turbulence in these conditions.

The present study would benefit from further investigations, particularly to locate the neutral point associated to the 1^{st} Mack mode and streaks, from quantities available in the Resolvent framework. Such considerations are the subject of ongoing work.

Acknowledgements

The author would like to thank Sébastien Esquieu for providing the data used to compare the Resolvent to the PSE Analysis in Section 5. This work was financially supported by the French Ministry of Armed Forces – Defence Innovation Agency (AID).



References

- [1] Horvath T. and Berry S. "Discrete-roughness transition for hypersonic flight vehicles". In: *Journal of Spacecraft and Rockets* 45.2 (2008), pp. 216–227. DOI: 10.2514/1.30970.
- [2] Fedorov A. "Transition and Stability of High-Speed Boundary Layers". In: *Annu. Rev. Fluid Mech.* 43 (2011), pp. 79–95. DOI: 10.1146/annurev-fluid-122109-160750.
- [3] Schneider S.P. "Hypersonic laminar-turbulent transition on circular cones and scramjet forebodies". In: *Progress in Aerospace Sciences* 40 (2004), pp. 1–50. DOI: 10.1016/j.paerosci.2003. 11.001.
- [4] Mack L.M. Boundary-Layer Linear Stability Theory. Tech. rep. 709. Jet Propulsion Laboratory, California Institute of Technology: AGARD, 1984.
- [5] Zhou J. and Cao W. "Effects of Entropy-Layer on the Boundary Layer over Hypersonic Blunt Cones considering Entropy Swallowing". In: *Physics of Fluids* 33.7 (2021). DOI: 10.1063/5.0053345.
- [6] Stetson K.F. and Rushton G.H. "Shock Tunnel Investigation of Boundary-Layer Transition at M = 5.5". In: *AIAA Journal* 5.5 (1967).
- [7] Softley E.J. Transition of the hypersonic boundary layer on a cone: Part ii—experiments at Mach 10 and more on blunt cone transition. Tech. rep. GE Space Science Lab, 1968.
- [8] Malik M.R., Spall R.E., and Chang C.L. "Effects of Nose Bluntness on Boundary Layer Stability and Transition". In: 28th Aerospace Science Meeting. High Technology Corporation. 1990, p. 112.
- [9] Paredes P. et al. "Nose-Tip Bluntness Effects on Transition at Hypersonic Speeds". In: *Journal of Spacecrafts and Rockets* 56.2 (2019), pp. 369–387. DOI: 10.2514/1.A34277.
- [10] Paredes P., Choudhari M.M., and Li F. "Mechanism for frustum transition over blunt cones at hypersonic speeds". In: *Journal of Fluid Mechanics* 894.22 (2020). DOI: 10.1017/jfm.2020.261.
- [11] Esquieu S. et al. "Flow and Stability Analysis of a Hypersonic Boundary Layer over an Axisymmetric Cone-Cylinder-Flare Configuration". In: *AIAA SciTech Forum*. 2019. DOI: 10.2514/6.2019-2115.
- [12] Van Ingen J. A suggested semi-empirical method for the calculation of the boundary layer transition region. Tech. rep. Delft University of Technology, 1956.
- [13] Smith A.M.O. and Gamberoni N. *Transition, Pressure Gradient and Stability Theory*. Tech. rep. Douglas Aircraft Company, 1956.

- [14] Chu B.-T. "On the Energy Transfer to Small Disturbances in Fluid Flow: part 1". In: Act. Mech 3.1
- [15] Bugeat B. et al. "3D Global Optimal Forcing and Response of the Supersonic Boundary Layer". In: Journal of Computational Physics 398.108888 (2019). DOI: 10.1016/j.jcp.2019.108888.
- [16] Caillaud C. et al. "Global stability analysis of a hypersonic cone-cylinder-flare geometry". In: 57th 3AF International Conference on Applied Aerodynamics. 2023, p. 112. URL: https://arxiv. org/abs/2303.16325.
- [17] Caillaud C. et al. "Separation and Transition on a Cone-Cylinder-Flare: Computational Investigations". In: AIAA Journal 63.7 (2025), pp. 2615–2634, DOI: 10.2514/1.J064221.
- [18] Poulain A. et al. "BROADCAST: A high-order compressible CFD toolbox for stability and sensitivity using Algorithmic Differentiation". In: Computer Physics Communications 283.108557 (2023). DOI: 10.1016/j.cpc.2022.108557.
- [19] Demetriades A. "Hypersonic Viscous Flow over a Slender Cone Part 3: Laminar Instability and Transition". In: AIAA Journal 535.74 (2025).
- [20] Blasius H. "Grenzschichten in Fliissigkeitenmit kleiner Reibung (The Boundary Layers in Fluids with Little Friction)". In: Zeitschrift fuer Mathematik und Physik 56.1 (1908).
- [21] Hernandez V. et al. Krylov-Schur Methods in SLEPc. Tech. rep. Universitat Politècnica de València, 2007.
- [22] Forrester A.I.J., Sóbester A., and Keane A.J. Engineering Design via Surrogate Modelling: A Practical Guide. Chichester, United Kingdom: John Wiley and Sons, 2008.
- Sipp D. and Marquet O. "Characterization of noise amplifiers with global singular modes: the case of the leading-edge flat-plate boundary layer". In: Theoretical and Computational Fluid Dynamics. Vol. 27. 5. 2013, pp. 617-635. DOI: 10.1007/s00162-012-0265-y.
- Johnson H. and Candler G. "Hypersonic Boundary Layer Stability Analysis Using PSE-Chem". In: 35th AIAA Fluid Dynamics Conference and Exhibit. DOI: 10.2514/6.2005-5023. eprint: https: //arc.aiaa.org/doi/pdf/10.2514/6.2005-5023. URL: https://arc.aiaa.org/doi/abs/10. 2514/6.2005-5023.
- [25] Lei J. and Zhong X. "Linear Stability Analysis of Nose Bluntness Effects on Hypersonic Boundary Layer Transition". In: Journal of Spacecraft and Rockets 49.1 (2012).